UCSF

UC San Francisco Previously Published Works

Title

Magnetic Particle Imaging for Highly Sensitive, Quantitative, and Safe in Vivo Gut Bleed Detection in a Murine Model.

Permalink

Journal

Authors

Yu, Elaine

Chandrasekharan, Prashant

Berzon, Ran

et al.

Publication Date

DOI

Peer reviewed

Magnetic Particle Imaging for Highly Sensitive, Quantitative and Safe *In Vivo* Gut Bleed Detection in a Murine Model

Elaine Y. Yu[†,@], **Prashant Chandrasekharan**[†,@], **Ran Berzon**[†], **Zhi Wei Tay**[†], **Xinyi Y. Zhou**[†], **Amit P. Khandhar**[‡], **R. Matthew Ferguson**[‡], **Scott J. Kemp**[‡], **Bo Zheng**[†], **Patrick W. Goodwill**[¶], **Michael F. Wendland**[†], **Kannan M. Krishnan**[‡,§], **Spencer Behr**[||], **Jonathan Carter**[⊥], and **Steven M. Conolly**[†,#]

[†]Department of Bioengineering, University of California, Berkeley, California 94720, United States

[‡]Lodespin Labs LLC, Seattle, Washington 98103, United States

[¶]Magnetic Insight, Inc., Alameda, California 94501, United States

[§]Department of Materials Science, University of Washington, Seattle, Washington 98195, United States

[||]Department of Radiology and Biomedical Imaging, University of California San Francisco, California 94143, United States

[⊥]University of California San Francisco Medical Center, California 94143, United States

[#]Department of Electrical Engineering and Computer Sciences, University of California, Berkeley, California 94720, United States

Abstract

Gastrointestinal (GI) bleeding causes more than 300,000 hospitalizations per year in the United States. Imaging plays a crucial role in accurately locating the source of the bleed for timely intervention. Magnetic Particle Imaging (MPI) is an emerging clinically translatable imaging modality that images superparamagnetic iron-oxide (SPIO) tracers with extraordinary contrast and sensitivity. This linearly quantitative modality has zero background tissue signal and zero signal depth attenuation. MPI is also safe: there is zero ionizing radiation exposure to the patient and clinically approved tracers can be used with MPI. In this study, we demonstrate the use of MPI along with long-circulating, PEG-stabilized SPIOs for rapid *in vivo* detection and quantification of GI bleed. A mouse model genetically predisposed to GI polyp development (Apc$^{Min/+}$) was used for this study, and heparin was used as an anticoagulant to induce acute GI bleeding. We then injected MPI-tailored, long-circulating SPIOs through the tail vein, and tracked the tracer biodistribution over time using our custom-built high resolution field-free line (FFL) MPI scanner. Dynamic MPI projection images captured tracer accumulation in the lower GI tract with excellent

contrast. Quantitative analysis of the MPI images show that the mice experienced GI bleed rates between 1 and 5 μL/min. Although there are currently no human scale MPI systems, and MPI-tailored SPIOs need to undergo further development and evaluation, clinical translation of the technique is achievable. The robust contrast, sensitivity, safety, ability to image anywhere in the body, along with long-circulating SPIOs lends MPI outstanding promise as a clinical diagnostic tool for GI bleeding.

Graphical abstract
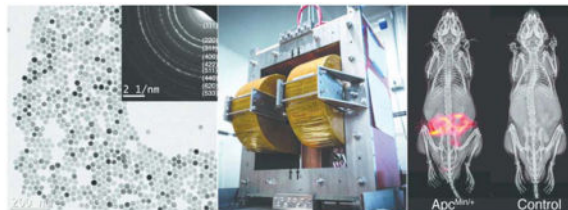
Keywords

magnetic particle imaging; gastrointestinal bleeding; medical imaging; blood pool contrast; superparamagnetic iron oxide nanoparticles

Gastrointestinal (GI) bleeding is a serious clinical problem and a common cause of hospitalization. Hospital admissions for GI bleeding in the United States and United Kingdom have been estimated at up to 150 per 100,000 population per year with a mortality rate of 5–10%.[1] GI bleeding is a diagnostic challenge both in its acute presentation, which requires the bleeding site to be located quickly, and in its chronic presentation, which requires repeated examinations to determine its etiology.[2,3] Accurate and timely diagnosis is essential in order to reduce morbidity, mortality, length of hospitalization and transfusion requirements.[4,5]

Established techniques for diagnosing lower GI bleeding include colonoscopy, CT angiography, catheter angiography, and radionuclide scintigraphy.[6] Colonoscopy has the highest efficacy in assessing major bleeding events in the lower GI tract.[7] However, accurate diagnosis requires bowel preparation (3–4 hours[2]) to empty contents of the colon. Additionally, colonoscopy is unable to examine most of the small bowel and introduces risks associated with sedation, perforation and increased bleeding.[1] CT angiography (CTA) is commonly used as it is widely available, does not require bowel preparation, and is minimally invasive. Catheter angiography is an invasive technique that is used with the added advantage of therapeutic intervention capabilities at the time of diagnosis. With the advent of spiral and multi-detector CT technology, the detection limit of lower GI bleed rate through CTA has been improved to 0.35–0.4 mL/min.[8–10] CT is also particularly useful for diagnosing hematomas as a result of trauma.[11] However, the sensitivity of CTA for diagnosis of GI bleeding has been shown to be higher in patients with active hemorrhage (91–92%) than in those with obscure GI bleeding (45–47%).[10] Due to decreased sensitivity, need for intravenous contrast material and a relatively high radiation dose, contrast-enhanced multi-detector CT has limited utility in cases of intermittent hemorrhage.[12]

The most sensitive imaging modality for GI bleeding is radionuclide imaging, with a bleed rate detection threshold of 0.05–0.2 mL/min and has a reported sensitivity of 93% and specificity of 95%.[13,14] Radionuclide scintigraphy for GI bleeding is either done with technetium-99m (^{99m}Tc) sulfur colloid or ^{99m}Tc-labeled red blood cells (RBC). ^{99m}Tc-sulfur colloid requires no preparation and can be directly injected into the patient. However, ^{99m}Tc-sulfur colloid has a short blood half-life (2–3 min), which means the patient must be actively bleeding during the period of observation, and repeated scanning for intermittent bleeding is not possible without re-injection.[4] ^{99m}Tc-labeled RBC scan is the preferred scintigraphic technique for lower GI bleeding detection due to the long blood half-life which allows the tracer to be detected on images for up to 24 hours after administration.[15] ^{99m}Tc-labeled RBC scans can detect active and intermittent bleeding with 80–98 % sensitivity.[3,16] However, a minimum extravasated bleed volume of 3–5 mL is required for detection irrespective of the bleed rate.[17]

Magnetic Particle Imaging (MPI),[18–22] is an emerging tracer imaging modality that directly measures the location and concentration of superparamagnetic iron-oxide nanoparticles (SPIO) *in vivo*. MPI is linearly quantitative and highly sensitive, detecting nanograms of iron (200 labeled cells) per voxel, which is equivalent to 130 nM.[23,24] As a comparison, the sensitivity of CT, MRI, and nuclear medicine techniques to contrast agents and tracers are in the millimolar, micromolar, and picomolar ranges, respectively.[25,26] The current resolution with MPI-tailored SPIOs[27,28] is ~1 mm, but may be improved to   300 μm resolution with optimized nanoparticles and pulse sequences.[29,30] Due to the low frequency magnetic fields used in MPI, there is zero signal depth attenuation and zero signal from the tissue itself. When the SPIO tracer is used as a blood pool agent, tissue perfusion and tracer extravasation is clearly visualized anywhere in the body. In addition to using no ionizing radiation, iron-oxide tracers with biocompatible coatings are safe and some are clinically approved as MRI contrast agents.[31] Hence, it is safe to repeat serial scans on an animal or human. At present, no human MPI scanner has been developed, but the commercial small animal MPI scanners are comparable in complexity to MRI scanners, so clinical translation should be feasible. The superb contrast, sensitivity, safety, and ability to image anywhere in the body gives MPI great promise for various blood pool imaging applications, including GI bleed detection.

In MPI, a time-varying homogeneous excitation field is applied during signal generation, causing SPIOs to instantaneously flip, thereby inducing a signal in the receive coil. A field-free region (FFR) is created with a strong magnetic gradient to localize the signal – only the particles at the FFR are able to flip and generate signal. The FFR is rastered through the field of view (FOV), and the signal detected is assigned to an image location corresponding to the instantaneous location of the FFR.[32] The field-free region can be a field-free point (FFP) or a field-free line (FFL). To image a 3D FOV, an FFP is rastered in all 3 dimensions, whereas an FFL can be rastered in 2 dimensions to create 2D projections of the volume, increasing imaging speed.[33] 3D volumes can also be made with an FFL scanner by taking projections at different angles and reconstructing with a filtered back projection algorithm,[34,35] akin to CT. A custom-built 6.3 T/m FFL MPI scanner[36] was used for this study. The dynamic *in vivo* projection imaging process is illustrated in Figure 1(a).

In this proof-of-concept study, we demonstrate that MPI could provide a noninvasive complement to ^{99m}Tc RBC scintigraphy for GI bleed detection with promising efficacy, as well as improvements in speed and radiation safety. We used the Apc$^{Min/+}$ mouse as a disease model of GI bleeding. Apc^{Min} (Min, multiple intestinal neoplasia) is a point mutation in the murine homolog of the adenomatous polyposis coli (APC) gene.[37] This mutation is often found in patients of familial adenomatous polyposis (FAP), a hereditary form of colon cancer. Polyps spontaneously develop in these mice with age, causing them to bleed and become anemic.[38,39] Heparin was used to induce acute bleeding at the beginning of the MPI study. Long circulating MPI-tailored SPIO tracer was then administered as a blood pool agent, and the animals were monitored with MPI over the course of 130 minutes. We implemented a high spatial and temporal resolution dynamic MPI projection scanning method to quantitatively detect GI bleeding *in vivo*. Due to the high contrast inherent to MPI, we captured clear images of the nanoparticle dynamics in the blood pool and nanoparticle extravasation into the gut lumen. The high contrast images also enabled quantitation of the blood flow rate into the gut.

Results and discussion

Projection Magnetic Particle Imaging Linearity and Detection Limit

A phantom containing SPIO tracer solutions of five different concentrations (0.0625–2 mg/mL, or 1.1–35.8 mM, each 10 μL) was imaged with MPI at two different projection angles. The projection at 0-degrees resulted in a line image, while the projection at 90-degrees resulted in a point image. 2D Projection-MPI was linearly quantitative ($r^2 = 0.99$), and the detected signal summations were consistent across projection angles, as shown in Figure 1(b). A conservative estimate puts the sample with the lowest tracer concentration (0.0625 mg/mL, 1.1 mM) at $15\times$ the detection limit of our system. The sample tubing had an inner radius of 0.53 mm (less than our imaging resolution), and was 9.2 mm in length, covering roughly 11.5 imaging voxels. From this, the system detection limit was calculated to be 3 ng Fe/voxel, which is equivalent to 670 nM for a pixel size of 0.1 $\times$ 0.2 cm and projected over 4 cm (80 μL). However, in order for the bleed to be detectable, it needs to stand out from existing perfused tissue signal in the abdomen. The signal in the abdomen from the control mice compared to background had a signal to noise ratio (SNR) of 17.2. Therefore, we estimate a final SNR of 50 ($3\times$ the perfused tissue signal) for the bleed to be detectable. Based on the injected dose of 5 mg Fe/kg (89.5 μmol Fe/kg) with 1.6 mL total blood volume, and assuming final SNR of 50, 2 μL of blood extravasating the gut lumen in one voxel is sufficient for our system to detect.

MPI-tailored Superparamagnetic Iron-Oxide Nanoparticles (SPIOs)

A bright field TEM image of uncoated iron oxide cores of LS-017 and (inset) Selected Area Diffraction pattern capturing crystal morphology and characteristic spinel diffraction rings are shown in Figure 2(a). A histogram of the core size as measured from the bright field TEM images is shown in Figure 2(b). Hydrodynamic size of the particles obtained from dynamic light scattering measurements was 89.3 nm with a polydispersity index (PDI) of 0.084. The magnetization curve was measured by VSM at room temperature, as shown in

Figure 2(c). The size of the ferromagnetic core, contributing to the MPI signal, was fit to a Langevin function and determined to be 28.7 nm.

Visualizing Gut Bleed with Dynamic Projection MPI

The experimental plan is illustrated in Figure 7 along with hematocrit levels measured for each group over time (right). Dynamic projection MPI studies were carried out when the hematocrit level of each $Apc^{Min/+}$ mouse became around 30–35% (aged 11–13 weeks), indicating active blood loss. Age matched wild-type C57BL/6 mice with hematocrit of ∼45% were used as control. PEGylated long-circulating SPIOs and heparin were injected through the tail vein as a bolus, and the dynamic projection MPI study was performed. Representative MPI images were overlaid with projection X-ray for anatomical reference, as shown in Figure 3. Whole body tracer dynamics was clearly captured over time. The long-circulating SPIOs remained in the blood pool throughout the duration of the experiment, as observed by the strong signal from the heart in both $Apc^{Min/+}$ and control mice. The mean circulation half-life for $Apc^{Min/+}$ and control mice determined from the dynamic MPI data were 113.6 and 140.4 minutes, respectively. Delayed extravasation of the tracer was observed in the lower abdomen of the $Apc^{Min/+}$ mice with time, specifically into the distal parts of the small intestine and large intestine, whereas no tracer extravasation was seen in the control mice. To further delineate the bleed sites, the MPI images at the first time point were digitally subtracted from each image in the rest of the time course for each animal, with negative changes set to zero. The resulting difference images, as shown in Figure 4, are quantitative maps of positive tracer accumulation. The GI bleed was visualized with extraordinary contrast in the $Apc^{Min/+}$ mice, whereas wild-type mice did not exhibit any signs of GI bleed.

Gut Bleed Quantitation

The rate of tracer extravasation into the gut lumen was quantified with two methods: (1) Non-linear least squares (NLLS) iterative fitting, and (2) a graphical linear least squares (LLS) approach similar to Patlak fitting,[40] as shown in Figure 5(a). The flow rates were significantly different between the $Apc^{Min/+}$ and control groups for both fitting methods: NLLS method (p = 0.014) and Patlak LLS method (p = 0.007), as shown in Figure 5(b). Representative fit results are shown in Figure 5(c)–(f). The flow rates for all animals, along with hematocrit levels when the study was conducted, are tabulated in Table 1. Both fitting methods yield closely correlated estimates of bleed rates for each animal, with a maximum bleed rate of 4.25 μL/min.

ex vivo MPI and Histology

The GI tracts were excised from each mouse after the dynamic projection MPI study. The tracts were subsequently imaged with MPI to verify presence and location of accumulated tracer. Representative *ex vivo* MPI image and corresponding photograph are shown in Figure 6(a). Tracer accumulation was found to be intraluminal at parts of small intestine and large intestine. Quantitative comparisons were made between the *in vivo* and *ex vivo* MPI signal for all animals. Near unity slope of 0.98 was obtained for the linear fit ($r^2 = 0.98$). This demonstrates that MPI is reliable and gives consistent results *in vivo* and *ex vivo*. Representative histological images of $Apc^{Min/+}$ and control mice are shown in Figure 6(c)

and (d). The healthy control mice had well-ordered mucosal and serosal layers in their GI tracts, while the Apc$^{Min/+}$ mice had polyps along their intestinal lining. RBCs were observed within the gut lumen adjacent to a polyp, as seen in Figure 6(d). This confirms the GI bleeding that was observed in both *in vivo* and *ex vivo* MPI of Apc$^{Min/+}$ mice.

Here we present an *in vivo* report of dynamic 2D projection MPI for detection and quantitation of lower gastrointestinal gut bleed using a non-radioactive and long circulating PEGylated SPIO tracer. We used the Apc$^{Min/+}$ mouse model, which was suitable for this study due to its clinically relevant genetic defect that causes spontaneous development of intestinal polyps. Our study warranted the need for heparin administration to induce bleeding in the mouse model, though such agents are typically contraindicated clinically for lower GI bleed diagnosis. However, we do note that clinical agents to reduce the gut peristalsis in ^{99m}Tc scans, like glucagon, can also increase cardiac contraction and vasodilation and encourage bleeding.[41]

Unlike nuclear medicine techniques where tracer quantitation requires correction for tissue attenuation, tracer decay, and detector dead-time, MPI signal is linearly quantitative with SPIO concentration and is not affected by the tracer decay or tissue attenuation. The quantitative nature of MPI enabled us to implement compartmental modeling to determine the bleed rate, assuming irreversible tracer extravasation into the gut lumen. The nonlinear compartment model fitting correlated well with the graphical linear least squares Patlak plot fitting result.[40] One can realize the immediate power of MPI for quantitative parametric tracer analysis. We were able to detect bleed rate as slow as 1–5 μL/min. The iron content in the GI lumen measured by MPI was also consistent between *in vivo* and *ex vivo* images, demonstrating that MPI is a reliable quantitative imaging technique. MPI has a fundamental detection sensitivity in the nM – μM range, which is less sensitive than nuclear medicine (pM – nM range).[25] However, since SPIO tracer is safe, it has a much less stringent dose limitation compared to nuclear medicine. This is why MPI allows detection of 0.002 mL of blood, which is 10 times more sensitive than the 0.02 mL detection limit shown in a rat with planar scinigraphy using MPEG-PL-Tc-99m DTPA,[42] both at clinically relevant dosages. Moreover, these experiments were obtained on a custom-built, prototype MPI scanner, with engineered sensitivity far from the true physics limits. With optimized hardware and SPIOs, it is certain that MPI sensitivity could be dramatically improved.

Several SPIO tracers were designed and tested clinically as MR contrast agents. However, many of these tracers have since then been withdrawn from the clinical market. Two of these tracers, Ferucarbotran and Ferumoxytol, are still used in the clinic. Ferucarbotran (Resovist®, Bayer Healthcare), which was designed primarily for liver imaging, is currently approved for use in Japan. Ferumoxytol (marketed as Feraheme® in the US and Rienso® in Europe), is commercially available for treating anemia and is used off-label as an angiographic agent for MRI.[43,44] Both Resovist® and Feraheme® can be used as MPI tracers, although Resovist®generates significantly higher levels of signal than Feraheme®. With the development of MPI, we are optimistic that we could revive some of the previously FDA and EU approved SPIO agents for clinical use.[45] In addition, SPIO tracers are generally considered to be safe for use in patients diagnosed with chronic kidney disease (CKD), unlike iodine and gadolinium-based contrast agents used for CT and MRI.[46,47]

Phase 1 clinical studies using Resovist® as an MRI contrast agent have shown insignificant side effects at the dose range of 5–40 μmol Fe/Kg.[48] Feraheme® has a full therapeutic dose of 261.4 μmol Fe/kg for anemia.[46]

By tailoring the core size and shape of the SPIOs, we can significantly improve imaging resolution and sensitivity of MPI.[27,49,50] Further, by modifying the surface chemistry of SPIOs, we can fine tune their pharmacokinetics and biodistribution properties *in vivo*.[21,51,52] In this study, we were able to achieve a prolonged circulation half-life of 140 minutes by polyethylene glycol (PEG) surface functionalization. The long-circulating nature of the tracer enabled dynamic imaging of the GI bleed over the course of 130 minutes. Unlike $_{99m}$Tc-labeled RBC studies which require cumbersome *in vitro* labeling and hot chemistry,[53] we were able to introduce our radiation-free SPIOs directly into the mice and image immediately. Preliminary safety assessment of similar MPI optimized tracers is promising, since the biodistribution and clearance routes are analogous to clinically approved SPIO contrast agents which are cleared *via* the reticuloendothelial system[48] with no long-term renal involvement.[28] However, the clinical safety profile of each MPI-tailored SPIO tracer formulation will require rigorous evaluation before entering the first in human phase.

It should be noted that to date, rodent-sized MPI scanners have been developed, but MPI has not been scaled for use on humans.[54,55] There are several challenges and factors to consider for this scale-up, including resolution, sensitivity, as well as *dB/dt* and specific absorption rate (SAR) safety limits. The resolution of MPI is highly dependent on MPI-tailored SPIOs as well as the selection field gradient strength. The 6.3 T/m gradient yielding 1 mm resolution projection images with our murine MPI imager is realizable at the human scale: for example, a commercially available clinical 3 T MRI scanner has a 7.2 T/m maximum spatial gradient just outside its bore.[54,56] Further improvements to resolution below 300 μm are feasible through optimized nanoparticles and pulse sequences.[30] Based on reciprocity analysis assuming coil noise dominance,[19,57] we estimate the molar sensitivity to improve by ~30-fold as we scale from mouse to human for fixed digital matrix size. Additional sensitivity improvement is also possible through tracer and receive hardware optimization.[50,58] In terms of scanner safety limits, our MPI systems currently operate in the very low frequency (VLF) range, which renders magnetostimulation the dominant safety limit. Human magnetostimulation studies of the arm and leg with spatially homogeneous axial excitation field have been conducted[54,59,60] to predict safety limits at the full body scale. However, it is still crucial to evaluate the safety limits by conducting human-subject experiments with the desired imaging setup.

Since MPI uses zero ionizing radiation, and the SPIO tracer is safe even for use in CKD patients, one could also envision a tracer moiety that has an even more prolonged clearance half-life to enable continued patient monitoring. SPIOs can be encapsulated in PEGylated PRINT nanoparticles with circulation half-life of 19.5 hours[61] or in red blood cells with tracer life span in the mouse bloodstream prolonged to 12 days.[62] SPIO-labeled RBC MPI for detection of GI bleeding should allow imaging for as long as 12 days, instead of 24 hours as reported in ^{99m}Tc-labeled RBC studies due to radioactive decay. With GI bleeding being intermittent by nature, repeated MPI scans could be performed to monitor the patient over

longer periods of time with no tracer re-injection. This may significantly improve the accuracy of diagnosis, especially for cases of the occult and obscure GI bleeding which are currently highly challenging to diagnose and treat.[63] In addition, we have demonstrated that digital subtraction of baseline images from the rest of the images in the time course can dramatically improve image contrast.

Conclusions

In this study, we have shown highly sensitive detection of GI bleed in a murine model using MPI. Although much remains to be done for the clinical translation of MPI tracers and imager, MPI is a clinically translatable imaging modality with superb contrast, sensitivity, linear quantitation and safety, which may have promise as a rapid, zero-radiation complement to ^{99m}Tc RBC scintigraphy. We believe that one day MPI could be used in conjunction with CT or Ultrasound for cases where bleeding has ceased, to complement the current clinical workflow for cases of occult or obscure GI bleeding. Additionally, MPI/CT hybrid systems could harness the high detection sensitivity of MPI along with the high resolution anatomical information provided by CT to enable higher accuracy bleed detection and bleed site localization, which may ultimately reduce cost and improve outcome.

Methods

Animal Procedures

All animal procedures were conducted according to the National Research Councils Guide for the Care and Use of Laboratory Animals and approved by the Animal Care and Use Committee at UC Berkeley. Male C57BL/6-Apc$^{Min/+}$ (8-week old) were obtained from Jackson Laboratories (Bar Harbor, ME). Male C57BL/6 mice (11-week old) were obtained from a UC Berkeley Office of Laboratory Animal Care approved vendor as wild-type control. All animals were monitored weekly for behavior, body weight and hematocrit level changes until they reached an age of 13 weeks. Once every week, 10 μL of blood was drawn from the tail vein of each mouse, and the hematocrit level was measured with the AimStrip Hb Hemoglobin Test System obtained from Germaine Laboratories (San Antonio, TX). The experimental workflow and hematocrit levels for all animals are shown in Figure 7.

MPI-tailored Superparamagnetic Iron-Oxide Nanoparticles (SPIOs)

MPI-tailored SPIO tracer (LS-017, LodeSpin Labs) was synthesized[21,64,65] to achieve optimal resolution and blood circulation half-life. The SPIOs were synthesized by thermolysis of iron III oleate in 1-octadecene, with subsequent oxidation (1 % oxygen in argon) to achieve desired magnetic behavior.[66] For biocompatibility and long circulation, poly(maleic anhydride alt-1-octadecene) (PMAO)-PEG(20k) coatings were created by attaching 20 kDa Methoxy-PEG-amine (JenKem USA) to PMAO (Sigma) (30–50 kDa).[64] The SPIOs were then coated with the amphiphilic polymer coating and dispersed in PBS for characterization and animal studies.

Bright field TEM was performed at 200 keV to characterize nanoparticle morphology and size. Selected Area Electron Diffraction (SAED) was performed at 200 keV to characterize crystalline phase. Hydrodynamic size of the coated nanoparticles was measured in PBS

using Dynamic Light Scattering (DLS, Malvern ZetaSizer Nano ZS). Magnetic properties were measured by Vibrating Sample Magnetometer (VSM, Lake Shore Cryoronics). Magnetic size was determined by fitting of M(H) data to a Langevin function (following Chantrell's method[67]).

Dynamic *in vivo* Projection Magnetic Particle Imaging

A custom-built vertical-bore Field-Free Line (FFL) $6.3T/m/\mu_0$ magnetic particle imager was used for this study. The SPIOs were excited at a drive field frequency of 20.225 kHz and an excitation strength of 40 mTpp. The FFL is created and shifted by a pair of water-cooled gradient and shift coils with laminated iron returns. The FFL is created along the y-direction and electronically shifted in the x-direction as illustrated in Figure 1. The scanning bed was mechanically translated in the z-direction at 1 mm increments to complete the imaging trajectory shown.

MPI-tailored long circulating SPIO tracer (5 mg Fe/kg, 89.5 μmol Fe/kg) and heparin were administered through the tail vein of each animal prior to imaging. For reference, the range of dosages reported for human and small animal imaging studies in literature are 0.5–7.3 mg Fe/kg (8.95–130.72 μmol Fe/kg) and 0.0145–56 mg Fe/kg (0.26–1002.7 μmol Fe/kg), respectively.[31,46,51] Twenty-one projection scans were acquired for each animal over the course of ~130 minutes to capture *in vivo* tracer dynamics over time. All *in vivo* images were taken with respiratory gating, with a final field of view of 5.16 cm $\times$ 8.52 cm. All images were reconstructed using x-space MPI reconstruction algorithm.[19,33] Projection X-ray images were acquired with a XPERT cabinet X-ray system (KUB Technologies, Inc) following each MPI study for anatomical reference.

Projection Magnetic Particle Imaging Linearity and Detection Limit

To show that our 2D projection imaging method is linearly quantitative, we prepared a phantom of 5 different tubes filled with 10 μL of LS-017 particle solution at various concentrations (0.0625, 0.25, 0.5, 1 and 2 mg/mL, 1.1–35.8 mM, each 10 μL) and imaged it at two different projection angles to create a line image in the 0-degree projection and a point image in the 90-degree projection. The signal was summed around the phantom for both projections for comparison. The system detection limit was also estimated from this study.

Image Processing and Data Analysis

MPI Image Analysis—After x-space reconstruction of the MPI images, the dynamic MPI time courses were collected for each animal. To better visualize the bleed into the gastrointestinal lumen, the image of the first time point was subtracted from the rest of the images in the time course to create difference maps. Since the GI bleed should manifest only as a positive accumulation of tracer over time, all negative changes in the difference maps were set to zero.

A conversion factor from MPI signal to iron (μg Fe) mass was calculated from the aforementioned phantom study. This conversion factor was applied to all MPI images and

difference maps to create quantitative tracer distribution images for each animal. These images were overlaid with projection X-ray images for anatomical reference.

Flow Quantitation through Compartment Fitting—The blood plasma tracer concentration C_p was determined by the MPI signal from the ventricle of the heart. A region of interest (ROI) around the heart was created from the MPI image of the first time point of each animal, and the same mask was applied across the rest of the images in the time course to determine amount of tracer in the heart over time. To determine the amount of tracer extravasated into the gut lumen, a single ROI for each time series was created around the gut using all the difference images, ensuring that all the areas of bleed are captured over time. For the control mice with minimal to no tracer extravasation over time in the gut, the original MPI image was used to draw an ROI around the gut. This ROI mask was then applied across all the difference images to determine the amount of tracer accumulated in the gut over time as a comparison. All image processing and analysis was performed using MATLAB (Mathworks, Natick, MA).

Two methods were implemented to quantify the bleed rate in the gut lumen (a) a nonlinear least squares method involving compartmental fitting (NLLS) and (b) and a graphical linear least squares (LLS) Patlak plot approach assuming an irreversible tracer extravasation into the gut lumen. A two compartment model was used for quantifying the rate of gut bleed. The two compartments represent the central blood pool compartment (vascular compartment) and the peripheral gut lumen compartment (irreversible compartment). The tracer exits the blood through two pathways: (1) Elimination due to nanoparticle filtration by the reticular-endothelial system (RES) and (2) Extravasation into the gut lumen due to bleeding. For the NLLS compartmental fitting, the tracer mass in the central blood pool compartment was calculated from the signal in the heart by assuming the heart volume to be 140 μL, and entire blood pool volume of each mouse V_0 to be 1.6 mL. Equations used for both methods are included as supporting information.

ex vivo MPI and Histology

The animals were euthanized immediately after the dynamic MPI study, and the GI tracts were extracted and imaged with MPI to confirm tracer presence. ROI analysis was conducted on all *ex vivo* GI tract MPI images, and the *in vivo* and *ex vivo* MPI signal of the GI tracts were compared.

After *ex vivo* MPI, the GI tracts were washed and subsequently fixed in neutral buffered formalin (NBF) and transfered to 70% ethanol after 24 hours. For each animal, GI tracts were separated into 4 segments: stomach, small intestine, cecum, and large intestine. The stomach and cecum were embedded into one paraffin block. Individual swiss rolls were created for the small and large intestines, and both rolls were embedded together into one paraffin block. Five micron sections were cut from each sample and Hematoxylin and Eosin (H & E) staining was performed on all slides. The slides were observed using an inverted bright field microscope (ZEISS AX10 Observer D1 with a ZEISS Axiocam ERc 5s).

Supplementary Material

Refer to Web version on PubMed Central for supplementary material.

Acknowledgments

References

1. Kim BSM, Li BT, Engel A, Samra JS, Clarke S, Norton ID, Li AE. Diagnosis of Gastrointestinal Bleeding: A Practical Guide for Clinicians. World J Gastrointest Pathophysiol. 2014; 5:467–478. [PubMed: 25400991]

2. Quiroga Gómez S, Pérez Lafuente M, Abu-Suboh Abadia M, Castell Conesa J. Gastrointestinal Bleeding: The Role of Radiology. Radiol. 2011; 53:406–420.

3. McDonald M, Ziessman H. Gastrointestinal Bleeding Scintigraphy. Appl Radiol. 2016; 45:19–22.

4. Vernava AM, Moore BA, Longo WE, Johnson FE. Lower Gastrointestinal Bleeding. Dis Colon Rectum. 1997; 40:846–858. [PubMed: 9221865]

5. Farrell JJ, Friedman LS. Review Article: The Management of Lower Gastrointestinal Bleeding. Aliment Pharmacol Ther. 2005; 21:1281–1298. [PubMed: 15932359]

6. Ramaswamy RS, Choi HW, Mouser HC, Narsinh KH, McCammack KC, Treesit T, Kinney TB. Role of Interventional Radiology in the Management of Acute Gastrointestinal Bleeding. World J Radiol. 2014; 6:82–92. [PubMed: 24778770]

7. Bounds BC, Friedman LS. Lower Gastrointestinal Bleeding. Gastroenterol Clin North Am. 2003; 32:1107–1125. [PubMed: 14696299]

8. He B, Yang J, Xiao J, Gu J, Chen F, Wang L, Zhao C, Qian J, Gong S. Diagnosis of Lower Gastrointestinal Bleeding by Multi-Slice CT Angiography: A Meta-Analysis. Eur J Radiol. 2017; 93:40–45. [PubMed: 28668429]

9. Wu LM, Xu JR, Yin Y, Qu XH. Usefulness of CT Angiography in Diagnosing Acute Gastrointestinal Bleeding: A Meta-Analysis. World J Gastroenterol. 2010; 16:3957–3963. [PubMed: 20712058]

10. Geffroy Y, Rodallec MH, Boulay-Coletta I, Julls MC, Ridereau-Zins C, Zins M. Multidetector CT Angiography in Acute Gastrointestinal Bleeding: Why, When, and How. Radiographics. 2011; 31:E35–E46. [PubMed: 21721196]

11. Lee EW, Laberge JM. Differential Diagnosis of Gastrointestinal Bleeding. Tech Vasc Interv Radiol. 2004; 7:112–122. [PubMed: 16015555]

12. Zink SI, Ohki SK, Stein B, Zambuto DA, Rosenberg RJ, Choi JJ, Tubbs DS. Noninvasive Evaluation of Active Lower Gastrointestinal Bleeding: Comparison Between Contrast-Enhanced MDCT and 99mTc-Labeled RBC Scintigraphy. AJR Am J Roentgenol. 2008; 191:1107–1114. [PubMed: 18806152]

13. Dusold R, Burke K, Carpentier W, Dyck WP. The Accuracy of Technetium-99m-Labeled Red Cell Scintigraphy in Localizing Gastrointestinal Bleeding. Am J Gastroenterol. 1994; 89:345–348. [PubMed: 8122642]

14. Grady E. Gastrointestinal Bleeding Scintigraphy in the Early 21st Century. J Nucl Med. 2016; 57:252–259. [PubMed: 26678616]

15. Holder LE. Radionuclide Imaging in the Evaluation of Acute Gastrointestinal Bleeding. Radiographics. 2000; 20:1153–1159. [PubMed: 10903704]

16. Kester RR, Welch JP, Sziklas JP. The 99mTc-Labeled RBC Scan. A Diagnostic Method for Lower Gastrointestinal Bleeding. Dis Colon Rectum. 1984; 27:47–52. [PubMed: 6317306]

17. Currie GM, Kiat H, Wheat JM. Scintigraphic Evaluation of Acute Lower Gastrointestinal Hemorrhage: Current Status and Future Directions. J Clin Gastroenterol. 2011; 45:92–99. [PubMed: 20861799]

18. Gleich B, Weizenecker J. Tomographic Imaging Using the Nonlinear Response of Magnetic Particles. Nature. 2005; 435:1214–1217. [PubMed: 15988521]

19. Goodwill PW, Conolly SM. The X-space Formulation of the Magnetic Particle Imaging Process: 1-D Signal, Resolution, Bandwidth, SNR, SAR, and Magnetostimulation. IEEE Trans Med Imag. 2010; 29:1851–1859.

20. Weizenecker J, Gleich B, Rahmer J, Dahnke H, Borgert J. Three-Dimensional Real-Time *In Vivo* Magnetic Particle Imaging. Phys Med Biol. 2009; 54:L1–L10. [PubMed: 19204385]

21. Khandhar AP, Keselman P, Kemp SJ, Ferguson RM, Goodwill PW, Conolly SM, Krishnan KM. Evaluation of PEG-coated Iron Oxide Nanoparticles as Blood Pool Tracers for Preclinical Magnetic Particle Imaging. Nanoscale. 2017; 9:1299–1306. [PubMed: 28059427]

22. Yu EY, Bishop M, Zheng B, Ferguson RM, Khandhar AP, Kemp SJ, Krishnan KM, Goodwill PW, Conolly SM. Magnetic Particle Imaging: A Novel *In Vivo* Imaging Platform for Cancer Detection. Nano Lett. 2017; 17:1648–1654. [PubMed: 28206771]

23. Zheng B, von See MP, Yu E, Gunel B, Lu K, Vazin T, Schaffer DV, Goodwill PW, Conolly SM. Quantitative Magnetic Particle Imaging Monitors the Transplantation, Biodistribution, and Clearance of Stem Cells. In Vivo Theranostics. 2016; 6:291–301. [PubMed: 26909106]

24. Zheng B, Vazin T, Goodwill PW, Conway A, Verma A, Ulku Saritas E, Schaffer D, Conolly SM. Magnetic Particle Imaging Tracks the Long-Term Fate of *In Vivo* Neural Cell Implants with High Image Contrast. Sci Rep. 2015; 5:14055. [PubMed: 26358296]

25. James ML, Gambhir SS. A Molecular Imaging Primer: Modalities, Imaging Agents, and Applications. Physiol Rev. 2012; 92:897–965. [PubMed: 22535898]

26. Fass L. Imaging and Cancer: A Review. Mol Oncol. 2008; 2:115–152. [PubMed: 19383333]

27. Ferguson RM, Khandhar AP, Kemp SJ, Arami H, Saritas EU, Croft LR, Konkle J, Goodwill PW, Halkola A, Rahmer J, Borgert J, Conolly SM, Krishnan KM. Magnetic Particle Imaging with Tailored Iron Oxide Nanoparticle Tracers. IEEE Trans Med Imag. 2015; 34:1077–1084.

28. Khandhar AP, Ferguson RM, Arami H, Krishnan KM. Monodisperse Magnetite Nanoparticle Tracers for *In Vivo* Magnetic Particle Imaging. Biomaterials. 2013; 34:3837–3845. [PubMed: 23434348]

29. Bauer LM, Situ SF, Griswold MA, Samia ACS. Magnetic Particle Imaging Tracers: State-of-the-Art and Future Directions. J Phys Chem Lett. 2015; 6:2509–2517. [PubMed: 26266727]

30. Tay ZW, Hensley DW, Vreeland EC, Zheng B, Conolly SM. The Relaxation Wall: Experimental Limits to Improving MPI Spatial Resolution by Increasing Nanoparticle Core Size. Biomed Phys Eng Express. 2017; 3:035003. [PubMed: 29250434]

31. Wang YXJ. Superparamagnetic Iron Oxide Based MRI Contrast Agents: Current Status of Clinical Application. Quant Imaging Med Surg. 2011; 1:35–40. [PubMed: 23256052]

32. Goodwill PW, Conolly SM. Multidimensional X-Space Magnetic Particle Imaging. IEEE Trans Med Imag. 2011; 30:1581–1590.

33. Goodwill PW, Konkle JJ, Zheng B, Saritas EU, Conolly SM. Projection X-Space Magnetic Particle Imaging. IEEE Trans Med Imag. 2012; 31:1076–1085.

34. Konkle JJ, Goodwill PW, Carrasco-Zevallos OM, Conolly SM. Projection Reconstruction Magnetic Particle Imaging. IEEE Trans Med Imag. 2013; 32:338–347.

35. Konkle JJ, Goodwill PW, Saritas EU, Zheng B, Lu K, Conolly SM. TwentyFold Acceleration of 3D Projection Reconstruction MPI. Biomed Tech. 2013; 58:565–576.

36. Yu, E., Zheng, B., Tay, ZW., Keselman, P., Zhou, X., Orendorff, R., Hensley, DW., Ferguson, RM., Khandhar, AP., Kemp, SJ., Krishnan, KM., Goodwill, PW., Conolly, SM. *In Vivo* Projection Imaging and 3D Computed Tomography Magnetic Particle Imaging with a High Resolution 6 T/m Field Free Line Electromagnet. World Molecular Imaging Congress; 2016;

37. Moser AR, Mattes EM, Dove WF, Lindstrom MJ, Haag JD, Gould MN. ApcMin, A Mutation in the Murine Apc Gene, Predisposes to Mammary Carcinomas and Focal Alveolar Hyperplasias. Proc Natl Acad Sci. 1993; 90:8977–8981. [PubMed: 8415640]

38. Wei H, Shang J, Keohane C, Wang M, Li Q, Ni W, O'Neill K, Chintala M. A Novel Approach to Assess the Spontaneous Gastrointestinal Bleeding Risk of Antithrombotic Agents Using Apc(min/+) Mice. Thromb Haemost. 2014; 111:1121–1132. [PubMed: 24430131]

39. Moser AR, Pitot HC, Dove WF. A Dominant Mutation that Predisposes to Multiple Intestinal Neoplasia in the Mouse. Science. 1990; 247:322–324. [PubMed: 2296722]

40. Patlak CS, Blasberg RG, Fenstermacher JD. Graphical Evaluation of Blood-to-Brain Transfer Constants from Multiple-Time Uptake Data. J Cereb Blood Flow Metab. 1983; 3:1–7. [PubMed: 6822610]

41. Saremi F, Jadvar H, Siegel ME. Pharmacologic Interventions in Nuclear Radiology: Indications, Imaging Protocols, and Clinical Results. Radiographics. 2002; 22:477–490. [PubMed: 12006682]

42. Gupta H, Weissleder R, Bogdanov AA, Brady TJ. Experimental Gastrointestinal Hemorrhage: Detection with Contrast-Enhanced MR Imaging and Scintigraphy. Radiology. 1995; 196:239–244. [PubMed: 7784574]

43. Molecular Imaging and Contrast Agent Database (MICAD) [Internet]. National Center for Biotechnology Information (US); Bethesda (MD): 2004–2013. Available from: https://www.ncbi.nlm.nih.gov/books/NBK5330/

44. Hope MD, Hope TA, Zhu C, Faraji F, Haraldsson H, Ordovas KG, Saloner D. Vascular Imaging with Ferumoxytol as a Contrast Agent. Am J Roentgenol. 2015; 205:W366–W373. [PubMed: 26102308]

45. Wang YX. Current Status of Superparamagnetic Iron Oxide Contrast Agents for Liver Magnetic Resonance Imaging. World J Gastroenterol. 2015; 21:13400–13402. [PubMed: 26715826]

46. Vasanawala SS, Nguyen KL, Hope MD, Bridges MD, Hope TA, Reeder SB, Bashir MR. Safety and Technique of Ferumoxytol Administration for MRI. Magn Reson Med. 2016; 75:2107–2111. [PubMed: 26890830]

47. Lu M, Cohen MH, Rieves D, Pazdur R. FDA report: Ferumoxytol for Intravenous Iron Therapy in Adult Patients with Chronic Kidney Disease. Am J Hematol. 2010; 85:315–319. [PubMed: 20201089]

48. Reimer P, Balzer T. Ferucarbotran (Resovist): A New Clinically Approved RES-Specific Contrast Agent for Contrast-Enhanced MRI of the Liver: Properties, Clinical Development, and Applications. Eur Radiol. 2003; 13:1266–1276. [PubMed: 12764641]

49. Ferguson RM, Khandhar AP, Arami H, Hua L, Hovorka O, Krishnan KM. Tailoring the Magnetic and Pharmacokinetic Properties of Iron Oxide Magnetic Particle Imaging Tracers. Biomed Tech. 2013; 58:493–507.

50. Ferguson RM, Minard KR, Khandhar AP, Krishnan KM. Optimizing Magnetite Nanoparticles for Mass Sensitivity in Magnetic Particle Imaging. Med Phys. 2011; 38:1619–1626. [PubMed: 21520874]

51. Arami H, Khandhar A, Liggitt D, Krishnan KM. *In Vivo* Delivery, Pharmacokinetics, Biodistribution and Toxicity of Iron Oxide Nanoparticles. Chem Soc Rev. 2015; 44:8576–8607. [PubMed: 26390044]

52. Keselman P, Yu E, Zhou X, Goodwill P, Chandrasekharan P, Ferguson RM, Khandhar A, Kemp S, Krishnan K, Zheng B, Conolly S. Tracking Short-Term Biodistribution and Long-Term Clearance of SPIO Tracers in Magnetic Particle Imaging. Phys Med Biol. 2017; 62:3440–3453. [PubMed: 28177301]

53. Srivastava SC, Chervu LR. Radionuclide-Labeled Red Blood Cells: Current Status and Future Prospects. Semin Nucl Med. 1984; 14:68–82. [PubMed: 6233700]

54. Saritas EU, Goodwill PW, Croft LR, Konkle JJ, Lu K, Zheng B, Conolly SM. Magnetic Particle Imaging (MPI) for NMR and MRI Researchers. J Magn Reson. 2013; 229:116–126. [PubMed: 23305842]

55. Mason EE, Cooley CZ, Cauley SF, Griswold MA, Conolly SM, Wald LL. Design Analysis of an MPI Human Functional Brain Scanner. Int J Magn Part Imaging. 2017; 3:1703008. [PubMed: 28752130]

56. Shellock FG, Kanal E, Gilk TB. Regarding the Value Reported for the Term "Spatial Gradient Magnetic Field" and How This Information Is Applied to Labeling of Medical Implants and Devices. AJR Am J Roentgenol. 2011; 196:142–145. [PubMed: 21178059]

57. Hoult DI, Lauterbur PC. The Sensitivity of the Zeugmatographic Experiment Involving Human Samples. J Magn Reson. 1979; 34:425–433.

58. Zheng B, Goodwill PW, Dixit N, Xiao D, Zhang W, Gunel B, Lu K, Scott GC, Conolly SM. Optimal Broadband Noise Matching to Inductive Sensors: Application to Magnetic Particle Imaging. IEEE Trans Biomed Circuits Syst. 2017; 11:1041–1052. [PubMed: 28742047]

59. Saritas EU, Goodwill PW, Conolly SM. Effects of Pulse Duration on Magnetostimulation Thresholds. Med Phys. 2015; 42:3005–3012. [PubMed: 26127053]

60. Demirel OB, Saritas EU. Effects of Duty Cycle on Magnetostimulation Thresholds in MPI. Int J Magn Part Imaging. 2017; 3:1703010.

61. Perry JL, Reuter KG, Kai MP, Herlihy KP, Jones SW, Luft JC, Napier M, Bear JE, DeSimone JM. PEGylated PRINT Nanoparticles: The Impact of PEG Density on Protein Binding, Macrophage Association, Biodistribution, and Pharmacokinetics. Nano Lett. 2012; 12:5304–5310. [PubMed: 22920324]

62. Antonelli A, Sfara C, Battistelli S, Canonico B, Arcangeletti M, Manuali E, Salamida S, Papa S, Magnani M. New Strategies to Prolong the *In Vivo* Life Span of Iron-Based Contrast Agents for MRI. PLoS One. 2013; 8:e78542. [PubMed: 24223101]

63. McKusick KA, Froelich J, Callahan RJ, Winzelberg GG, Strauss HW. 99mTc Red Blood Cells for Detection of Gastrointestinal Bleeding: Experience with 80 Patients. AJR Am J Roentgenol. 1981; 137:1113–1118. [PubMed: 6976077]

64. Khandhar AP, Ferguson RM, Arami H, Kemp SJ, Krishnan KM. Tuning Surface Coatings of Optimized Magnetite Nanoparticle Tracers for *In Vivo* Magnetic Particle Imaging. IEEE Trans Magn. 2015; 51:5300304. [PubMed: 25904816]

65. Krishnan, KM. Fundamentals and Applications of Magnetic Materials. 1. Vol. 1. Oxford University Press; 2016. p. 1

66. Kemp SJ, Ferguson RM, Khandhar AP, Krishnan KM. Monodisperse Magnetite Nanoparticles with Nearly Ideal Saturation Magnetization. RSC Adv. 2016; 6:77452–77464.

67. Chantrell R, Popplewell J, Charles S. Measurements of Particle Size Distribution Parameters in Ferrofluids. IEEE Trans Magn. 1978; 14:975–977.
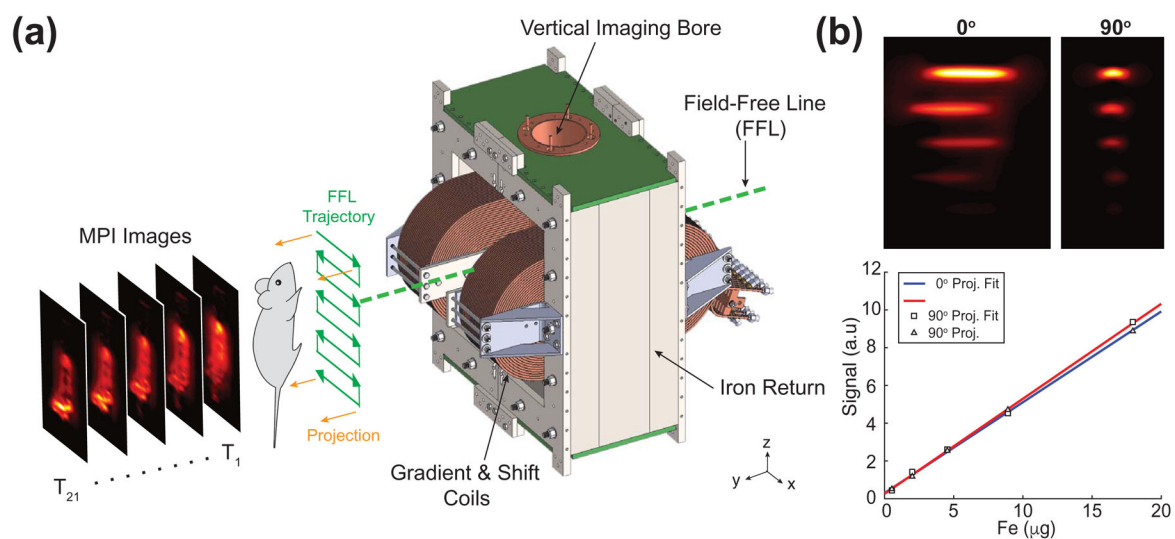
**Figure 1. Custom-built vertical bore 6.3 T/m Field-Free Line scanner**
(a) The FFL is rastered across the imaging field of view, and 2D projection images are acquired over time. (b) *Top:* MPI images of a concentration phantom (5 concentrations ranging from 0.0625 to 2 mg Fe/mL, each 10 μL in thin tubing spanning ~1 cm) at two different projection angles. The 0° projection resulted in a line image, while the 90° projection resulted in a point image. *Bottom:* MPI is linearly quantitative ($r^2 = 0.99$), and the total detected signal was consistent between projection angles (red, 90°, blue, 0°).
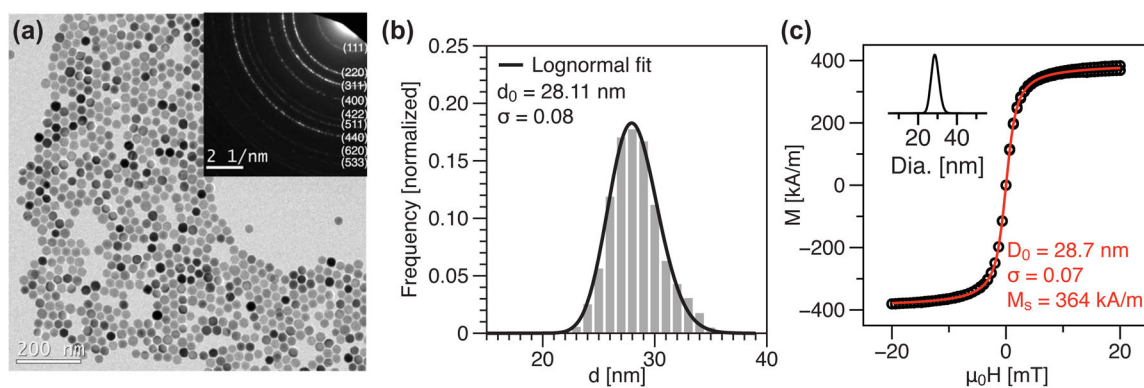
Figure 2. Long circulating MPI-tailored SPIO tracer

(a) Bright field TEM image of uncoated iron oxide cores of LS-017 and (inset) Selected Area Electron Diffraction pattern showing crystal morphology and characteristic spinel diffraction rings. (b) Histogram of particle core size from bright field TEM (mean = 28.11, σ = 0.08). (c) Magnetization curves measured by VSM at room temperature. Magnetic size was 28.7 nm (σ = 0.07). This figure was adapted from Nano Lett. 2017, 17, 1648–1654.[22]
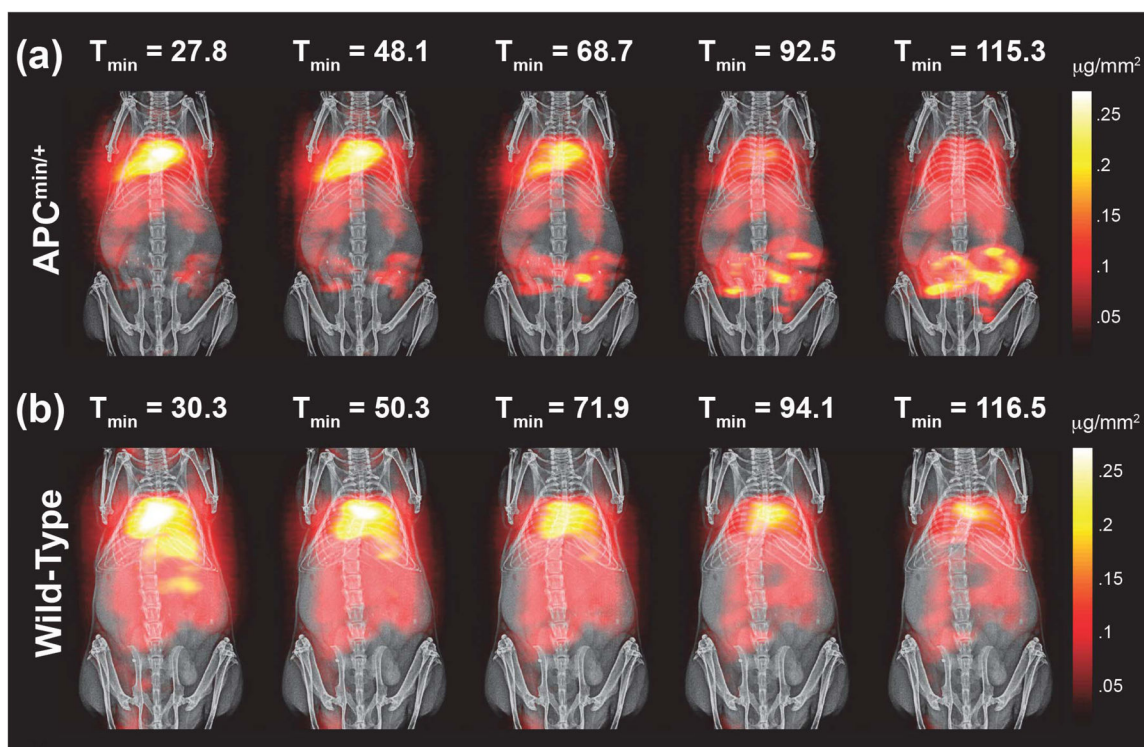
Figure 3. Dynamic projection MPI captures whole body tracer bio-distribution
MPI co-registered with projection X-ray for anatomical reference. (a) Representative images of an Apc$^{Min/+}$ mouse over time. MPI clearly captures dynamics of tracer extravasation into the gut. (b) Representative images of a Wild-Type mouse over time. No tracer extravasation into the gut is seen.
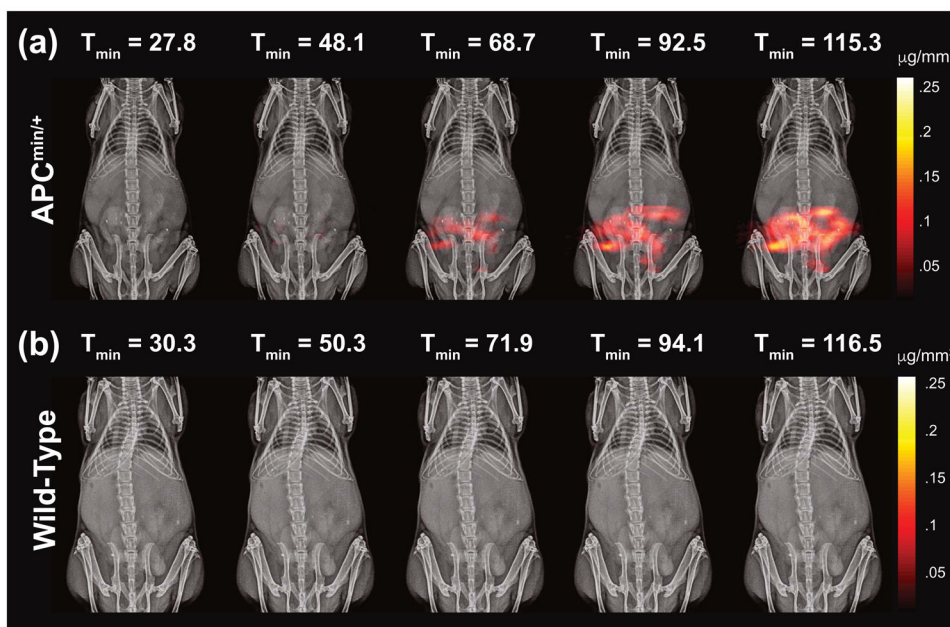
Figure 4. MPI Subtraction Images

Each MPI image was further processed by digital subtraction. The MPI image at the first time point was subtracted from all remaining images in the time course to capture tracer accumulation. (a) Representative subtracted images of an Apc$^{Min/+}$ mouse over time. The GI bleed is visualized with extraordinary contrast. (b) Representative subtracted images of a wild-type mouse over time. The tracer was predominantly in the blood pool throughout the study, hence not observed after subtraction. Additionally, no GI bleed is observed.
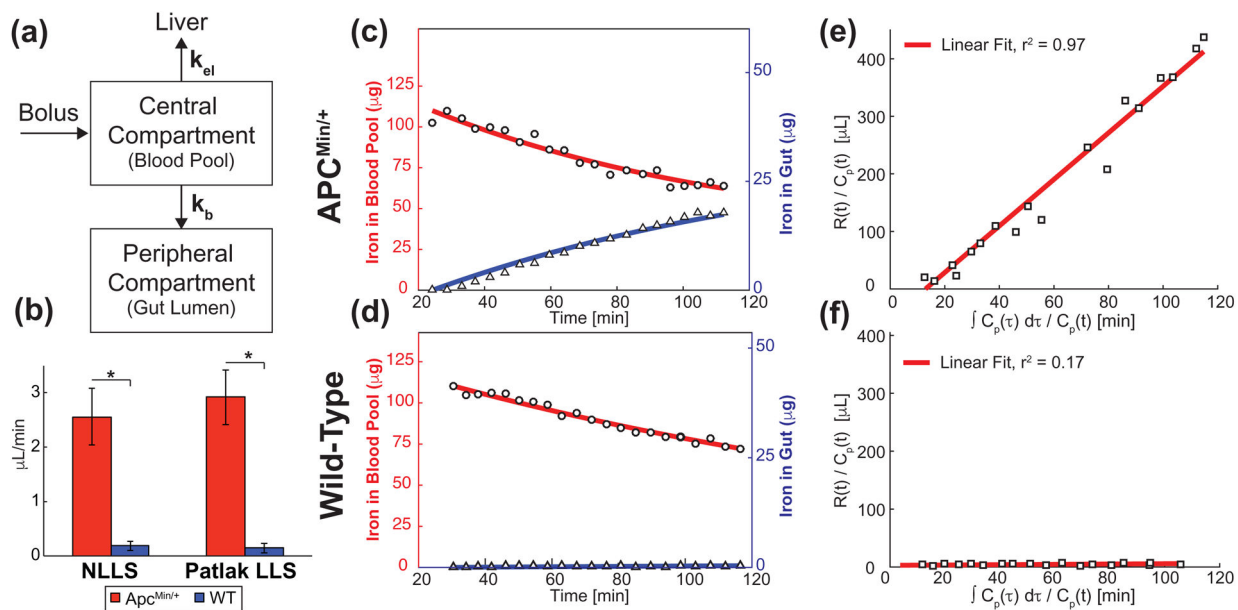
Figure 5. Gut Bleed Flow Quantitation

(a) Schematic of two compartment model used to quantify the rate of bleed into the gut. (b) Bar graph of flow rate from both groups. The flow rates were significantly different between the Apc$^{Min/+}$ and wild-type groups for both fitting methods: NLLS method (p = 0.014) and patlak LLS method (p = 0.007). Representative NLLS fit results for (c) Apc$^{Min/+}$ mice and (d) wild-type mice. Axes: iron in blood on left and iron in gut lumen on right. Representative LLS Patlak fit results for (e) Apc$^{Min/+}$ mice and (f) wild-type mice.
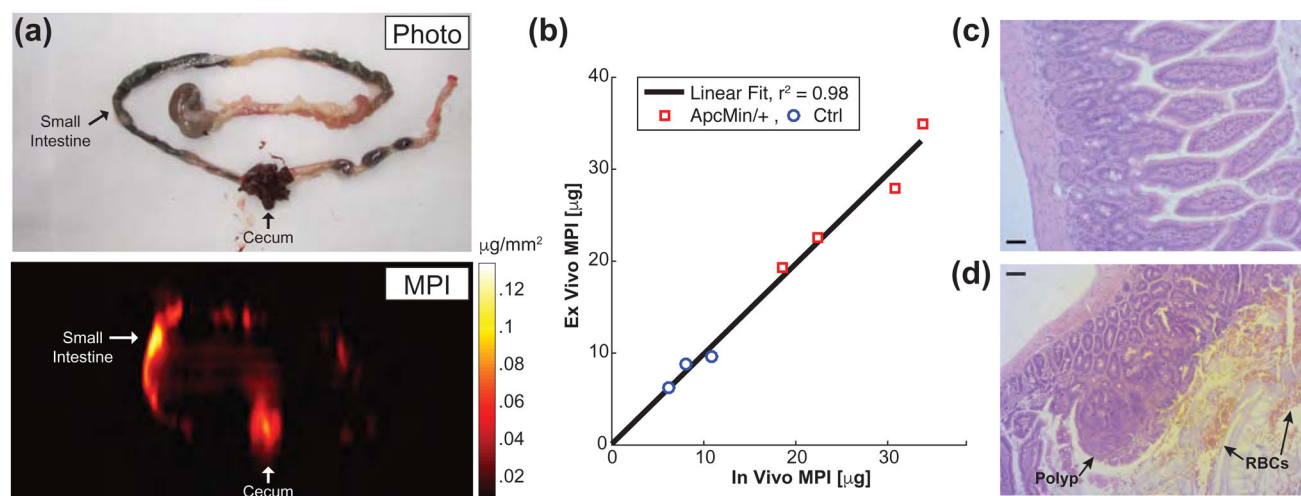
Figure 6. *Ex Vivo* MPI Scans
(a) Representative photo and corresponding MPI image of Apc$^{Min/+}$ mouse GI tract after dynamic MPI study. Tracer accumulation is seen in the cecum and small intestine. (b) *Ex vivo* and *in vivo* MPI signal from the gut were compared for all mice. Near unity slope of 0.98 was obtained for the linearity fit (r^2 = 0.98). H&E stained histological section of the intestinal lumen: (c) Control mouse with well-ordered mucosal and serosal layers (20× magnification, scale bar 50 μm) and (d) Apc$^{Min/+}$ mouse with a polyp along the intestinal lining and RBCs in the lumen (10× magnification, scale bar 100 μm).
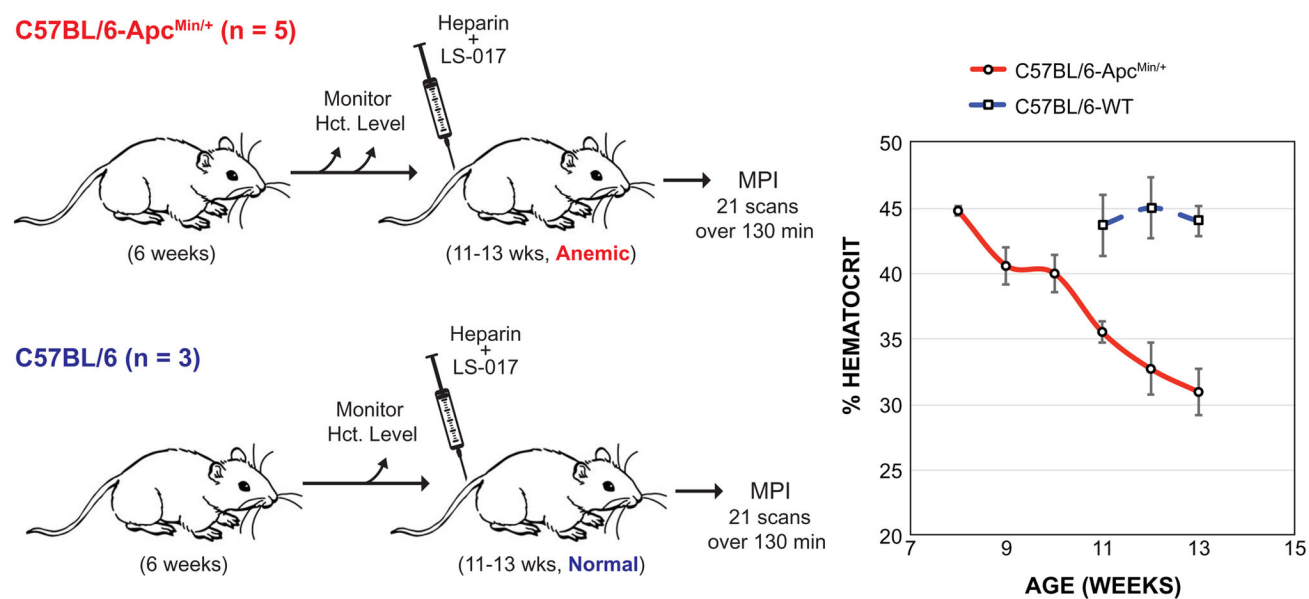
Figure 7. Experimental work-flow

C57BL/6-Apc$^{Min/+}$ mice (n = 5) and C57BL/6-WT mice (n = 3) were used for this study. Polyps spontaneously developed in the Apc$^{Min/+}$ mice with age, causing them to bleed and become anemic. The hematocrit levels were monitored weekly throughout the experiment. At age 11–13 weeks, anti-coagulant (Heparin) and MPI tracer (LS-017) were injected through the tail vein in both Apc$^{Min/+}$ and WT mice, followed by dynamic 2D projection MPI scans (21 projections over 130 minutes).

Table 1

Gut bleed flow rate comparison.

ID	Species	Hct (%)	NLLS Flow Rate (μL/min)	LLS Flow Rate (μL/min)
1	$Apc^{Min/+}$	30.18	2.01	2.39
2	$Apc^{Min/+}$	34.69	4.01	4.25
3	$Apc^{Min/+}$	34.57	1.55	1.97
4	$Apc^{Min/+}$	34.10	1.64	1.94
5	$Apc^{Min/+}$	N.A.	3.60	4.05
6	WT	42	0.34	0.32
7	WT	46	0.13	0.09
8	WT	44	0.07	0.03